



OPEN ACCESS

EDITED BY

Lijie Guo,
Beijing Mining and Metallurgy
Technology Group Co., Ltd., China

REVIEWED BY

Liang Cui,
Lakehead University, Canada
Erol Yilmaz,
Recep Tayyip Erdoğan University, Türkiye

*CORRESPONDENCE

Yongxiang Zhou,
✉ zhoyx@bjut.edu.cn

RECEIVED 08 March 2023

ACCEPTED 06 April 2023

PUBLISHED 14 April 2023

CITATION

Wang C, Qi Y, Jing J, Ma J, Zhou Y, Ping H,
Zheng Y, Zhai Y and Liu F (2023),
Properties and microstructure of total
tailings cemented paste backfill material
containing mining and metallurgical
solid waste.
Front. Earth Sci. 11:1181952.
doi: 10.3389/feart.2023.1181952

COPYRIGHT

© 2023 Wang, Qi, Jing, Ma, Zhou, Ping,
Zheng, Zhai and Liu. This is an open-
access article distributed under the terms
of the [Creative Commons Attribution
License \(CC BY\)](https://creativecommons.org/licenses/by/4.0/). The use, distribution or
reproduction in other forums is
permitted, provided the original author(s)
and the copyright owner(s) are credited
and that the original publication in this
journal is cited, in accordance with
accepted academic practice. No use,
distribution or reproduction is permitted
which does not comply with these terms.

Properties and microstructure of total tailings cemented paste backfill material containing mining and metallurgical solid waste

Changlong Wang¹, Yang Qi¹, Jianlin Jing¹, Jintao Ma¹,
Yongxiang Zhou^{2*}, Haoyan Ping¹, Yongchao Zheng³, Yuxin Zhai⁴
and Feng Liu⁵

¹Collaborative Innovation Center for Intelligent Regulation and Integrated Management of Water Resources Jointly Built by Provinces and Ministries, School of Civil Engineering, Hebei University of Engineering, Handan, China, ²Faculty of Architecture, Civil, and Transportation Engineering, Beijing University of Technology, Beijing, China, ³State Key Laboratory of Solid Waste Reuse for Building Materials, Beijing Building Materials Academy of Science Research, Beijing, China, ⁴Technical Center, China Railway Construction Group Co., Ltd., Beijing, China, ⁵Construction Development Co., Ltd., China Railway Construction Group, Baoding, China

Introduction: In order to improve the utilization efficiency of industrial waste discharged in the process of iron and steel metallurgy, a kind of material that can replace cement for mine filling is sought. In the test, steel slag (SS) and vanadium-titanium slag (VTS) were used as the primary raw materials to prepare cementing agents (CA). Then, combine it with vanadium-titanium iron ore tailings (VTIOTs) to make mine cemented paste backfill material (CPBM).

Methods: The composition, properties and hydration mechanism of CPBM are studied through various tests, including mechanical property test, hydration heat test, X-ray diffraction (XRD), scanning electronic microscopy (SEM), and fourier transform-infrared spectroscopy (FT-IR).

Results: The results show that when the following conditions are met, the slump is 216 mm, and the 28-day flexural strength and compressive strength of CPBM reach 4.25 and 9.41 MPa, respectively, which meets the requirements of Chinese National Standard GB/T 39489-2020 Technical specification for the total tailings paste backfill: the mass percentage SS: VTS: phosphogypsum (PG): dicyandiamide waste slag (DWS) = 31:59:6:4; the content of compound phosphoric acid (CPA) accounts for 4% of the dry material; the cement sand ratio of CPBM is 1:4; the paste mass concentration (PMC) is 80%; and the content of water reducing agent (WRA) is 0.18%.

Discussion: Mechanism studies show that the hydration product of the CA is mainly ettringite (AFt) and C-S-H gel. The addition of CPA promotes the hydration of active minerals in SS and VTS. The existence of PG promotes the formation of AFt, and the formation of AFt further promotes the fracture of $[AlO_4]^{5-}$ and $[SiO_4]^{4-}$ along the bridge oxygen in VTS and SS.

KEYWORDS

steel slag (SS), vanadium-titanium slag (VTS), cementing agent (CA), cemented paste backfill material (CPBM), ettringite

1 Introduction

With the rapid growth of the world's demand for mineral resources, people's requirements for environmental mining protection are increasing day by day, and mining equipment and technical level and gelling agent technical level are greatly improved (Wang F et al., 2020). Cemented paste backfill material (CPBM) is becoming a modern technology with high efficiency, strength, and recovery (Ghirian and Fall, 2016; Deng et al., 2017). Total-tailings CPBM, as a new mining technology, can return environmentally hazardous tailings to underground tunnels or stopes, which maximizes the safety and productivity of mining process operations. This is of great significance to solving the safety risks and environmental problems caused by a large accumulation of tailings (Su and Zhang, 2013; Yilmaz et al., 2014). Traditional CPBMs mostly use Portland cement as the cementing agent (Yilmaz et al., 2014; Ke et al., 2015; Yilmaz et al., 2015; Li and Fall, 2016). According to statistics, the cost of CPBM generally accounts for 25%–40% of the total mining cost, and the cost of cementing agent accounts for about 70%–80% of the filling cost (Li et al., 2011; Peyronnard and Benzaazoua, 2012). Therefore, how to develop suitable materials based on local conditions and local materials to replace cement materials is an important subject. It can reduce filling costs and determine the application prospect of filling mining technology.

At present, a lot of practical work has been carried out in China and abroad to find a substitute for cement materials. Metallurgical slag, as a kind of industrial solid waste, has certain cementitious properties and pozzolanic activity. Therefore, it has a great potential to prepare filling materials through mechanical milling and chemical activation, such as steel slag (SS) (Zhang et al., 2016), granulated blast furnace slag (GBFS) (Cihangir and Akyol, 2018), lead-zinc slag (Li et al., 2018) and copper-nickel slag (Zhang et al., 2020; Wu et al., 2018). Vanadium-titanium slag (VTS) and SS, as industrial residues during iron and steel metallurgy, have good potential activity after the activation of desulfurized gypsum 17–21 (Cho and Choi, 2016; Zhao et al., 2016; Ashrit et al., 2017; Duan et al., 2018; Jiang et al., 2018). Therefore, based on the studies on cementing materials of cement concrete, some researchers have begun to explore the use of SS and VTS to replace or partially replace cement in the preparation of cementing agent (CA) for CPBM (Zhang et al., 2016; Zhang et al., 2019a; Zhang et al.). In order to improve the performance of the system, so that the CPBM can be better used in practice, the experimenter selected solid waste powder different from the previous study, such as: SS, VTS, dicyandiamide waste slag (DWS), phosphogypsum (PG), and compound phosphoric acid (CPA). In this system, the experiment provided a large amount of SO_4^{2-} for the formation of C-S-H gels and ettringite by adding PG. On the one hand, the hydration of DWS could provide an alkaline environment for the reaction of the system; on the other hand, it could react with PG to convert harmful phosphorus and fluorine impurities into inert insoluble salts. On this basis, in order to improve the early strength characteristics of the material, CPA was used to modify the system. The addition of CPA promoted the consumption of $\text{Ca}(\text{OH})_2$, the activity of mineral powder and steel slag powder was further stimulated, and the hydration products increased in the early stage of the system. Then, vanadium-titanium iron ore tailings

(VTIOTs) are added to make total-tailings CPBM. The produced CPBM meets the conveying and strength requirements of backfill materials, and it has the characteristics of early strength, which can improve the filling mining efficiency.

All the materials used in the CPBM were solid wastes, which can greatly reduce the production cost of filling materials and improve the resource utilization of bulk industrial solid wastes such as SS, VTS, and VTIOTs. In this study, activated metallurgical slag was adopted as the main raw material to make CPBM. Then, various tests, including mechanical property test, X-ray diffraction (XRD), scanning electronic microscopy (SEM), and flourier transform-infrared spectroscopy (FT-IR), are conducted to explore its raw material composition and properties, and the effect of the amount of its raw materials and activators on the working performance and mechanical properties of CPBM. Besides, the hydration products of the CA are also studied.

2 Test materials and methods

2.1 Test materials

The test materials include SS, VTS, DWS, PG, CPA, and VTIOTs. Their chemical compositions are shown in Table 1.

2.1.1 SS

The SS used is the converter steel slag (without overheating treatment) with the chemical composition of f-CaO as 1.42% and f-MgO as 0.93%. The alkalinity value can reflect the activity of SS to a certain extent, and it is calculated through the Mason's method (Mason, 1944).

According to the alkalinity value, SS is classified as: low-alkalinity SS (<1.8), medium-alkalinity SS (1.8–2.5), and high-alkalinity SS (>2.5). The alkalinity value of the SS used in the test is 2.48 and it is medium-alkalinity SS. Moreover, the f-CaO content and alkalinity value of the SS meet the requirements of Chinese National Standard GB/T 20491-2017 Steel Slag Powder Used for Cement and Concrete, that is, f-CaO content $\leq 3\%$ and alkalinity value ≥ 1.8 . The particle size distribution analysis of the SS shows that 82.03% of the SS particles have the diameter between 0.3 mm and 9.5 mm. Thus, the SS should be broken before grinding. The major mineral phases of SS are C_3S , C_2S , RO phase (Figure 1A). According to BSE image analysis (Huo et al., 2021a), the used SS contains 18.78% glass phase by volume, 20.68% RO phase by volume, 58.14% silicate phase by volume and 2.40% SiO_2 , MgO, and other phases.

2.1.2 VTS

As can be seen from Table 1, the chemical composition of VTS is similar to that of ordinary GBFS. The main chemical components are SiO_2 , CaO, MgO, and Al_2O_3 . The content of CaO is low while that of TiO_2 is high, reaching 14.56%. The main mineral components are perovskite and merwinite (Figure 1B).

2.1.3 DWS

The dry base size of DWS is 0–0.1 mm, and the CaO content is 59.54%. The main mineral components are $\text{Ca}(\text{OH})_2(\text{CH})$ and CaCO_3 (see Figure 1C). The residue on the sieve with 0.08 mm square holes accounts for 12.8%.

TABLE 1 Chemical composition of raw materials (wt.%).

Materials	SiO ₂	Al ₂ O ₃	Fe ₂ O ₃	FeO	MgO	CaO	Na ₂ O	K ₂ O	SO ₂	TiO ₂	LOI
SS	15.71	5.86	13.58	6.22	8.59	43.69	0.10	0.06	0.64	—	1.67
VTS	23.47	11.12	2.48	0.02	12.20	33.05	0.52	0.40	0.99	14.56	1.11
DWS	3.45	1.94	0.078	0.29	—	59.54	0.28	0.001	3.55	—	30.11
PG	3.16	1.35	0.47	0.09	7.49	33.38	0.13	0.18	36.56	0.13	8.28
VTIOT	44.47	7.39	9.78	0.92	11.21	21.62	0.55	0.23	0.09	0.04	2.04

2.1.4 PG

PG is derived from Hubei Huangmailing Phosphoric Chemical Co., Ltd., which is gray powder with the particle size as 5–150 μm and the relative density as 2.31 g cm⁻³. The major components are CaSO₄·2H₂O and CaSO₄·1/2H₂O (Figure 1D).

2.1.5 VTIOTs

For the VTIOTs with the mass fraction of about 77.4%, the particle size is between 0.08 and 0.32 mm. The particles with more than 0.32 mm account for 14.5%, and those with less than 0.08 mm account for 8.1% (Table 2). The main mineral components are augite and hornblende, while the secondary mineral components are biotite, chlorite and ilmenite (Figure 1E). It can be seen from Figure 2 that the particle size of VTIOTs is mainly concentrated in the range of 0.3–1.18 mm, accounting for 64.43% (Figure 2).

2.1.6 Other materials

In the test, phosphoric acid (PA) is an analytical reagent, and the concentration is 85.0 wt.%. Anhydrous alcohol (AA) is also an analytical reagent and the concentration is no less than 99.5%. PA and AA are combined to prepare 80 wt.% CPA modified solution. The superplasticizer is polycarboxylates high performance water-reducing admixture (PC), and P-O 42.5 ordinary Portland cement (OPC) is used in the contrast test.

2.2 Test methods

Firstly, SS was broken into 1–3 mm particles by jaw crusher, and then the broken SS, VTS, DWS, PG were placed in the oven at 105°C for 24 h to make moisture content less than 1%, respectively. Secondly, they were milled with the SM φ 500 mm × 500 mm laboratory ball mill at the speed of 48 r min⁻¹ to yield specific surface area (SSA) after milling were 510, 540, 455, and 390 m² kg⁻¹, respectively. The grinding media consists of several steel balls and a steel forging. The loading mass of the grinding media should be 100 kg. The steel balls add up to 40 kg, in which the Φ70 mm ball takes up 19.7%, the Φ60 mm ball takes up 33.1%, the Φ50 mm ball takes up 29.6%, and Φ40 mm ball takes up 17.6%; the Φ25 mm ×30 mm steel forging weighs 40 kg.

When the pulverized raw materials were mixed evenly in proportion, some 80 wt.% CPA modified solution was dripped into the cement mortar mixer with the raw materials at the speed of 125 ± 10 r min⁻¹ for 8–15 min. After stirring for 2 h, the materials were put in an oven at 105°C for 2 h and the CA was obtained. Then, the CA was mixed with VTIOTs according to a

certain cement sand ratio, and some water was added. And we stirred the materials until a certain paste mass concentration (PMC) was reached. After stirring, the slurry was put into the cement mortar triple testing mold (40 mm × 40 mm × 160 mm) and it was vibrated on the cement mortar vibration platform. After 24 h, it was demoulded and put into a standard curing box with the temperature of (20 ± 1)°C and humidity of more than 90%. Finally, the mechanical properties of the test blocks at different ages were determined. By measuring the mechanical properties of the sample fillers, we obtained a set of the optimal ratio of the CA. XRD, FT-IR and SEM were used to analyze the CA paste hydration process.

2.3 Property characterization

Based on Chinese National Standard YB/T 140-2009 Methods of Chemical Analysis for Steel Slag, the f-CaO of SS was determined by EDTA complexometric titration with ethylene glycol as the extractant. According to Chinese national standard GB/T 19077-2016 Particle size analysis—Laser diffraction methods, we chose ethanol as the dispersant and analyzed the particle size distribution of ground steel slag by MASTER SIZER 2000 (a laser particle size analyzer with the analysis range between 0.02 and 2,000 μm). The SSA was measured using SSA-3200 dynamic specific surface area analyzer. For the test blocks at different ages, we tested their compressive strength according to Chinese National Standard GB/T 17671-2022 Method of testing cements—Determination of strength. The mechanical properties were tested by YES-300 digital hydraulic pressure testing machine. Its loading rate was (2.0 ± 0.5) kN/s and the maximum load was 300 KN. The slurry slump in the test was determined by referring to Chinese National Standard GB/T 50080-2016 Standard for Test Method of Performance on Ordinary Fresh Concrete.

For XRD analysis, Japan's neo-confucianism Rigaku D/MAX-RC 12 KW rotating anode diffractometer with Cu target was adopted whose working current was 150 mA and working voltage was 40 kV. It could generate rays with the wavelength of 1.5406 nm. The exothermic rate of hydration and the total heat of hydration were measured by Calmetrix isothermal calorimeter. The SEM observation was performed to analyze the hydration products of the CA samples using a Zeiss SUPRATM55 scanning electron microscope coupled with a Be4-U92 energy spectrum. The functional group's vibration of CA samples was qualitatively analyzed by NEXUS70 Fourier transform infrared (FT-IR, test range 350–4,000 cm⁻¹).

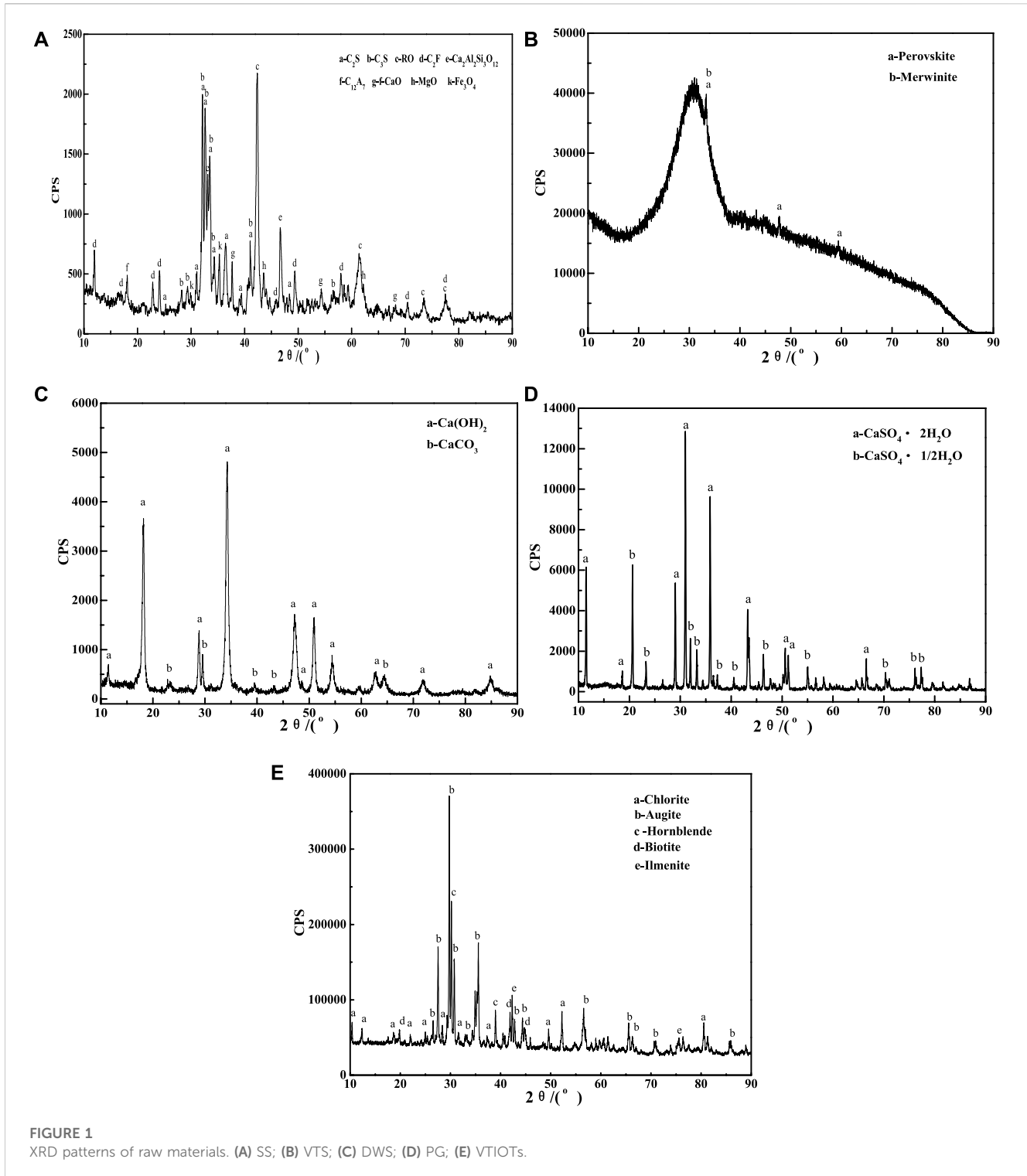


TABLE 2 Particle size distribution of VTIOTs.

Sieve size/mm	+1.25	-1.25	-0.63	-0.32	-0.16	-0.08
		+0.63	+0.32	+0.16	+0.08	
Meter sieve/%	1.7	6.1	6.7	36.1	41.3	8.1
Cumulative sieve/%	1.7	7.8	14.5	50.6	91.9	100

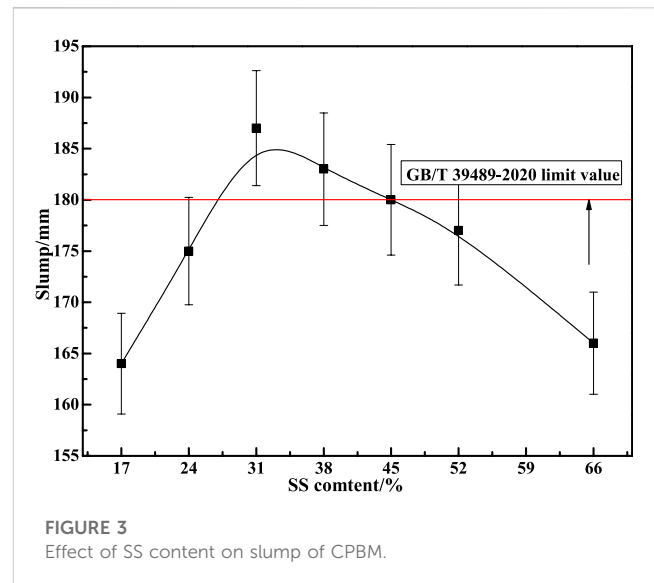
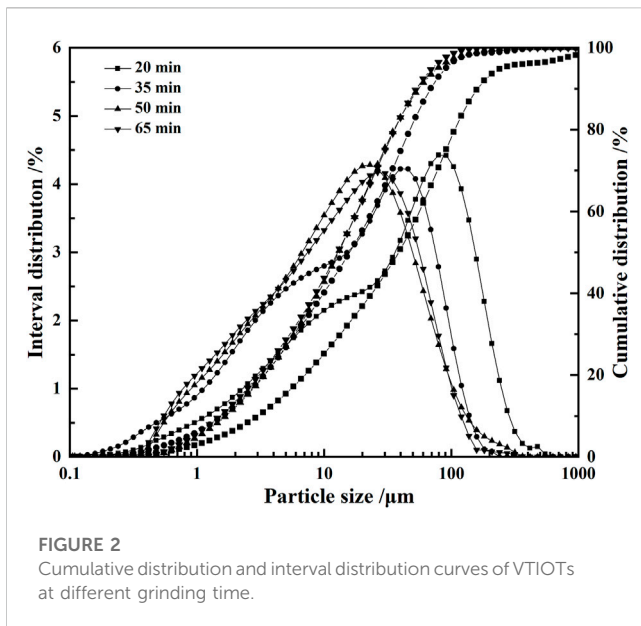


TABLE 3 Mix proportion of total-tailings CPBM.

Number	Composition of CA				Cement sand ratio	PMC/%
	SS%	VTS/%	DNS/%	PG/%		
C-1	17	77	1	9	1:4	79
C-2	24	66	3	7		
C-3	31	59	4	6		
C-4	38	52	5	5		
C-5	45	45	6	4		
C-6	52	38	8	2		
C-7	66	24	9	1		

Note: PMC = solid mass/(solid mass + liquid mass) × 100%.

3 Results and discussion

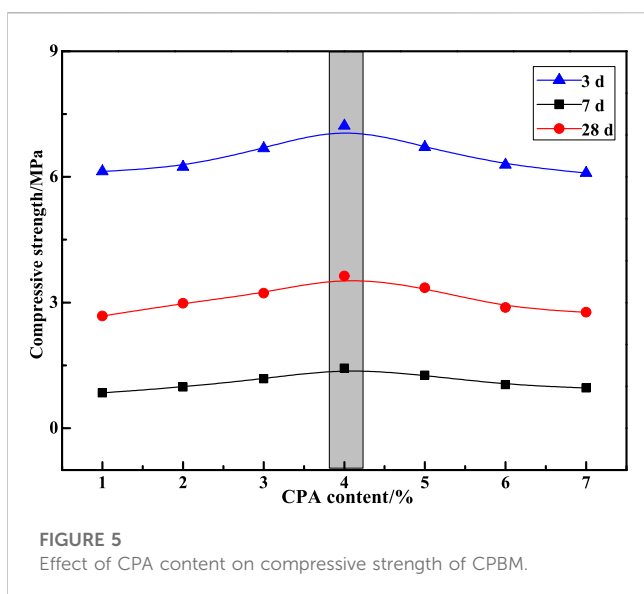
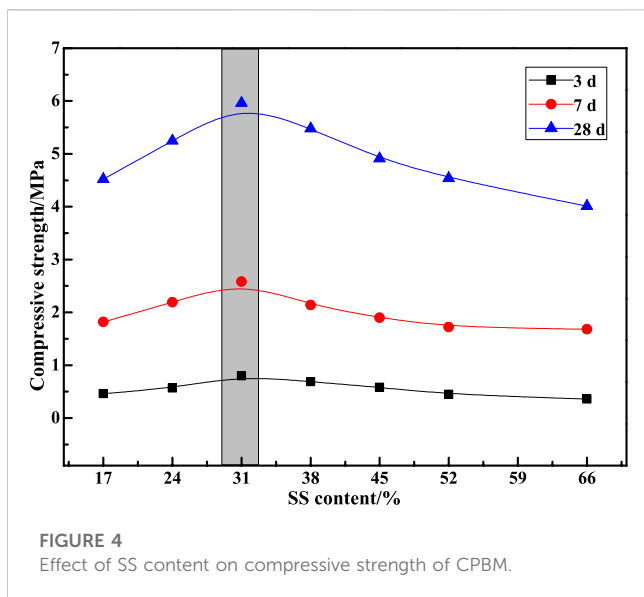
3.1 Effect of SS content on the properties of CPBM

SS contains a certain amount of C₃S and C₂S, and has certain gelling activity. Besides, VTS has a certain glass phase. Thus, SS and VTS can be used as cementing materials at the same time. With the activator, SS and VTS can activate each other. Therefore, the total content of SS, VTS, PG and DWS is 100% in the initial ratio tentatively. DWS belongs to the alkali activator while PG is the sulfate activator. Only when the two activators are added according to a reasonable proportion, can SS and VTS produce the best excitation effect. Based on our previous studies (Zhang et al., 2019a; Zhang et al., 2019b; Wang C et al., 2020; Wang et al., 2021), the total mass percentage of SS and VTS in the CA is set as 90% while that of PG and DWS is 10%. The SSA of SS and VTS after grinding are 510 and 540 m² kg⁻¹, respectively. The cement sand ratio is 1:4. The paste mass concentration (PMC) is 79%. The test ratio is shown in Table 3.

Figure 3 shows the influence of different SS contents on the slump value of CPBM. As seen in Figure 3, slurry fluidity first increases and then decreases with the increase of SS content. Slump value reaches 180 mm when SS content is 31%, 38%, and 45%. Figure 4 represents the influence of SS content on the compressive strength of the CPBM. It can be seen that the compressive strength of sample blocks at each age first increases and decreases then with the increase of SS content. The compressive strength reaches the maximum when the SS content is 31%.

The compressive strength of the CPBM samples at 3 d, 7 d and 28 d are 0.80, 2.58, and 5.96 MPa, respectively, and the slump reaches 187 mm, which meets the following requirements of Chinese national standard GB/T 39489-2020 Technical specification for the total tailings paste backfill: 180 mm ≤ slump value ≤ 260 mm; 0.2 MPa ≤ uniaxial compressive strength ≤ 5 MPa.

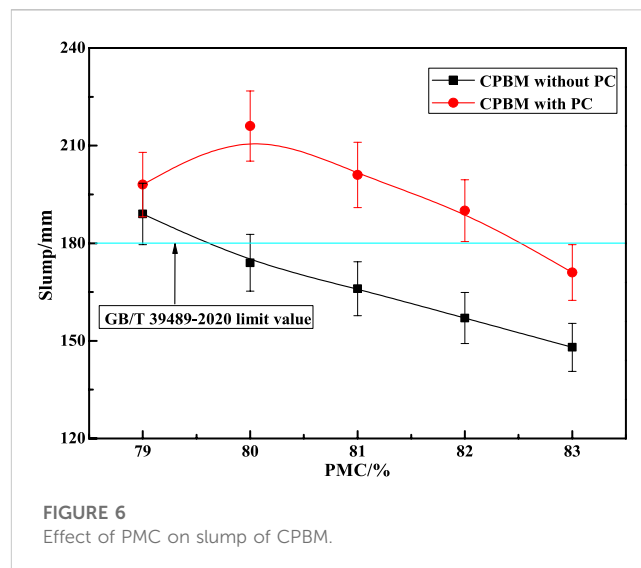
In this case, using metallurgical solid waste SS and VTS as the CA can generate environmental and ecological benefits which are in line with the national industrial policy. Therefore, C-3 was selected as the optimal formulation in the subsequent studies.



3.2 Effect of CPA content on the properties of CPBM

From Section 3.1, we can find that the cementitious activities of SS and VTS can be stimulated to a certain extent after being activated by mechanical force. However, the activation effect is limited, and the strength of the prepared CPBM is low. Therefore, CPA was selected as the auxiliary activator in this study, and its appropriate dosage was determined through experiments. Based on the mix proportion of C-3, the ratio of SS, VTS, DWS and PG in the CA was determined. Then, the CPA content was set from 1% to 7% of the CA, so as to investigate the influence of the CPA content on the properties of the CPBM. The results are shown in Figure 5.

It can be seen from Figure 5 that the compressive strength of CPBM reaches the highest value at 3 d, 7 d, and 28 d when the CPA content is 4%. When the mass fractions of SS, VTS, PG and DWS in



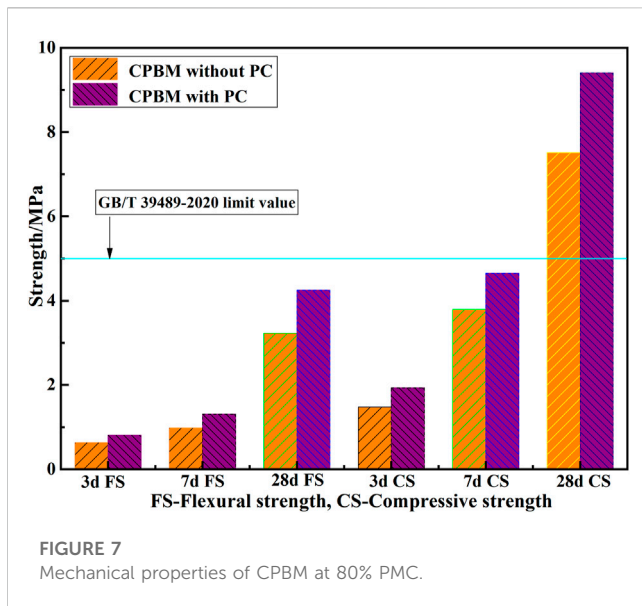
the CA are 31%, 59%, 6%, and 4%, respectively, the cement sand ratio is 1:4 and the PMC is 79%, the compressive strength of the CPBM is 1.43, 3.63, and 7.22 MPa at 3 d, 7 d, and 28 d, respectively. The compressive strength of the CPBM mixed with 4% CPA is increased by 78.8%, 40.7%, and 21.1% compared with that of the CPBM with no CPA at 3 d, 7 d, and 28 d, respectively. This is mainly because SS and VTS, as the products after high-temperature calcination, have dense connections among their mineral crystals (Fisher and Barron, 2019). After milling, the hydration of SS and VTS is slow, producing fewer hydration products. Therefore, the early activity of CA and the strength of CPBM are lower.

According to Huo et al. (2020) and Huo et al. (2021b), the surface roughness of SS and VTS modified by CPA, increases the SSA and porosity of the powder, which makes it easier for the surface of the powder to absorb water molecules. Meanwhile, water molecules can enter the interior of the powder particles through pore channels, which enables the active minerals in SS and VTS to have more contact with water molecules. As a result, they can participate in the hydration reaction and generate more hydration products. However, excessive CPA will delay the hydration process of active minerals in SS and VTS, decreasing the mechanical properties of CPBM.

3.3 Effect of PMC on the properties of CPBM

Usually, the PMC is 75%–88%. If the PMC is too large, the fluidity of the paste will become poor. If it is too small, the paste filling body will become layered and separated. Therefore, the PMC was set between 79% and 83%, and the mix proportion of optimized CA was SS: VTS: PG: DWS = 31:59:6:4. The cement sand ratio was 1: 4. Then, CPA (4% of the CA) and PC (0.18% of the CA) were added to determine the mechanic strength and slump of the CPBM. The test results are compared with the samples without PC (Figures 6, 7).

As can be seen from Figure 6, when the PMC is between 79% and 83%, the slump of the CPBM with PC is significantly higher than that without PC. Only when the PMC is 79% can the slump of the



latter one meet the slump index (189 mm) in Chinese National Standard GB/T 39489-2020 Technical Specification for the Total Tailings Paste Backfill. After adding PC, the slump of the CPBM increases significantly. When the PMC is between 79% and 82%, the slump value of the CPBM system is always higher than the lowest slump (180 mm) in GB/T 39489-2020. The maximum slump reaches 216 mm when the PMC is 80%.

With the increase of PMC, the slump decreases. The addition of PC is beneficial to improve the mechanical properties of the CPBM system. Figure 7 shows the mechanical properties of CPBM with the PMC of 80%. The 3 d, 7 d, and 28 d flexural strength and compressive strength of CPBM with PC are obviously better than those without PC.

The flexural strength of the CPBM samples with PC reaches 0.81, 1.31, and 4.25 MPa at 3 d, 7 d, and 28 d, respectively, increased by 28.6%, 33.7%, and 31.6% compared with those without PC at the same age. Meanwhile, the compressive strength reaches 1.93, 4.65, and 9.41 MPa at 3 d, 7 d, and 28 d, respectively, increased by 30.4%, 22.7%, and 25.3%. The flexural strength and compressive strength of the CPBM meet the strength index in Chinese National Standard GB/T 39489-2020 Technical Specification for the Total Tailings Paste Backfill. Compared with the filling requirements of most mines, the strength of CPBM in this study is higher. In application, the water-binder ratio and slump can be selected and adjusted according to the specific requirements of the mine for strength and pumping conditions.

3.4 Mechanism analysis

3.4.1 Hydration heat analysis

Figure 8 shows the hydration exothermic rate curve of cement slurry ($W/b = 0.50$) and CA ($W/b = 0.50$) measured by a TAM air 8-channel isothermal calorimeter (a precise temperature control within $\pm 0.02^\circ\text{C}$). In the test, the mix proportion of the optimized CA is SS: VTS: PG: DWS = 31:59:6:4 and the content of CPA accounts for 4% of the CA. During the test, they are placed in the

room at 25°C . By comparing the hydration exothermic process of the CA paste and the cement paste, it can be seen that the early hydration exothermic process of the CA can be divided into five stages: the CA dissolves rapidly in contact with water and releases much heat rapidly, thus forming the first exothermic peak, $24\text{--}26\text{ mW g}^{-1}\text{ h}^{-1}$ (Figure 8B). In order to make the curve clearer in the later stage, the maximum value of the vertical coordinate in Figure 8A is set to $8\text{ mW g}^{-1}\text{ h}^{-1}$.

This stage is called the early induction stage. The exothermic peak is formed mainly due to the release of surface energy when the powder is in contact with water. Only when the concentrations of Ca^{2+} and OH^- reach a critical value do the hydration products CH and C-S-H gel begin to crystallize from the solution. Therefore, after the first stage, the hydration is relatively inactive, which is called the induction phase.

Then comes the hydration acceleration phase. During this phase, the hydration reactions are most concentrated and intense, and CH and C-S-H gel are formed in large quantities. The hydration exothermic power of the CA reaches the second peak.

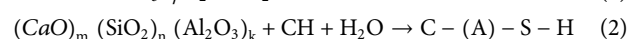
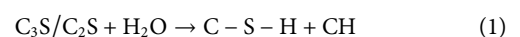
With the decrease of active substances in hydration, it enters the deceleration stage and the hydration exothermic power of the sample slowly decreases. C-S-H gel forms the wrapping layer around the paste particles as the hydration continues. The increasing thickness of the wrapping layer will make it harder for the water to pass through the layer and arrive at the remaining paste particles. Thus, the hydration becomes much slower, which is called the stable phase. During this phase, the hydration of C_2S and C_3S is controlled by the diffusion rate and becomes stable.

As can be seen from Figures 8C, D and Table 4, the exothermic rate of CA is significantly lower than that of pure cement during hydration. It is decreased by 68.56%, 78.16%, 65.02%, 47.21%, and 41.84% at the age of 12, 24, 36, 48, and 60 h, respectively. The main reason is that the hydration activity of CA is less than that of pure cement. Although PG, DWS and CPA are activated, the overall hydration activity is still lower than that of pure cement. When the hydration continues for 60 h, the maximum hydration heat release of the CA is only 58.16% of that of pure cement.

3.4.2 XRD analysis

Figure 9 shows the XRD pattern of the hydration products of the CA paste samples with the curing age of 3 d, 7 d, and 28 d, respectively. These samples are prepared according to the optimized CA content ratio and the water-binder ratio is 0.5.

In the above XRD patterns of the CA paste samples at 3 d, 7 d, and 28 d of standard curing, we can find ettringite (AFt), $\text{Ca}(\text{OH})_2$, RO phase, CaSO_4 , C_2F , $\text{Ca}_3(\text{PO}_4)_2$, CaCO_3 , and unhydrated C_3S and C_2S . SS is similar to cement clinker, in which active minerals C_3S and C_2S undergo hydration reaction to produce C-S-H gel and CH, and the reaction formula is shown as Eq. 1. In Figure 9, there is an obvious “bulging” at $25^\circ\text{--}35^\circ$, indicating that the system contains a large number of C-S-H gel and amorphous substances with low crystallinity (Bensted and Barnes, 2002; Wang et al., 2016; Wang et al., 2018). C-S-H gel is continuously deposited with the extension of curing age, which gradually thickens and hardens the slurry, thus rapidly increasing its macroscopic strength (Cui et al., 2017).



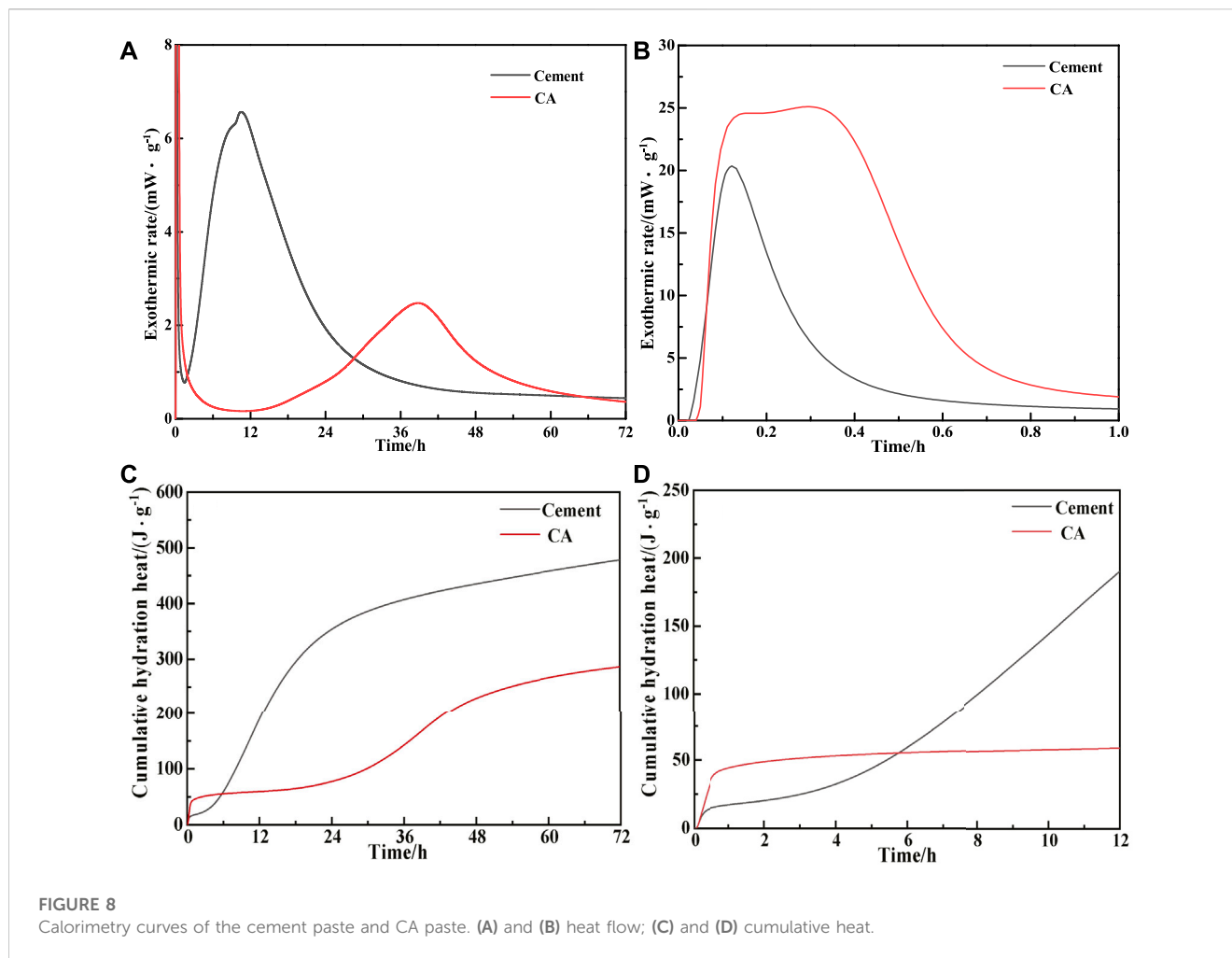


TABLE 4 Hydration rate and total exothermic of hydration at different hydration times.

Hydration time/h		12	24	36	48	60
Cement	hydration rate/(mW g ⁻¹)	6.21	1.94	0.81	0.56	0.50
	total exothermic/(J g ⁻¹)	188.98	354.21	407.30	435.41	458.03
CA	hydration rate/(mW g ⁻¹)	0.17	0.80	2.28	1.24	0.59
	total exothermic/(J g ⁻¹)	59.41	77.37	142.48	229.86	266.40

It is worth noting that amorphous vitreous [(CaO)_m (SiO₂)_n (Al₂O₃)_k] also exists in SS and VTS, which is proved by the steamed bun peaks between 25° and 40° (Figures 1A, B). Vitreous has volcanic activity (Mejdi et al., 2019). The reaction formula is shown in Eq. 2. Therefore, CH generated by the hydration of C₃S and C₂S in SS and CH in DWS will consume the glass phase of SS and VTS. As a result, the diffraction summit of C₃S and C₂S in Figure 9 will gradually weaken with the extension of curing age.

In Figure 9, AFt diffraction peaks appear at 2θ of 15.7°, 19.0°, 23.1°, and 32.3°, and the peaks gradually strengthen with the extension of curing age. Since the generation of AFt consumes the CaSO₄ in PG, the diffraction summit of CaSO₄ in hydration

products weakens with the extension of curing age (Li et al., 2017; Wu et al., 2019). Activated by gypsum sulfate and CPA, VTS are continuously hydrated. The cations such as Ca²⁺ and Mg²⁺ on the surface of VTS vitreous body first dissolve into the solution, and the charge imbalance between [SiO₄]⁴⁻ and [AlO₄]⁵⁻ intensifies, resulting in the break of Al-O bond of [AlO₄]⁵⁻ and dissolving out AlO₂⁻ from the vitreous surface. And a dissolution balance tends to occur between the vitreous surface and the solution. AFt is produced in the participation of free gypsum, improving the strength of the gel system.

With the continuous formation of AFt, the dissolution balance of AlO₂⁻ between the VTS vitreous surface and the solution is

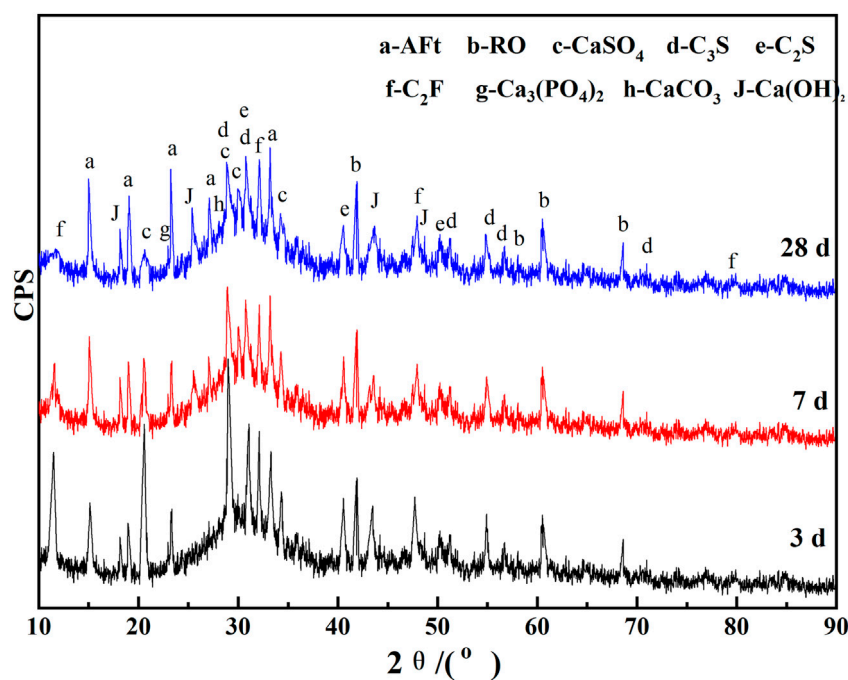


FIGURE 9
XRD pattern of CA paste samples at different ages.

constantly broken, which promotes the continuous migration of $[\text{AlO}_4]^{5-}$ from the VTS vitreous surface, so as to maintain the slag secondary hydration. The migration of $[\text{AlO}_4]^{5-}$ from the slag vitreous surface destroys the connection between $[\text{SiO}_4]^{4-}$ and $[\text{AlO}_4]^{5-}$. It results in a rapid decline in the polymerization degree of silicon (aluminum) oxygen tetrahedron on the VTS vitreous surface, and a significant increase in the activity of residual $[\text{SiO}_4]^{4-}$ and $[\text{AlO}_4]^{5-}$. C-S-H gel is continuously formed in CA solution with rich Ca^{2+} and they are continuously deposited, which gradually thickness and hardens the slurry, thus rapidly increasing the macroscopic strength. The sample used in the test has been enclosed in the centrifugal tube since it is formed. So, there is no CaCO_3 produced by carbonization. The mineral phase of CaCO_3 in Figure 9 is the mineral residue in DWS. RO phase basically does not participate in the hydration reaction of the system, so there is RO phase in the hardened slurry. After CPA is added to the CA system, the hydration of minerals in SS and VTS is accelerated. Thus, the mineral phase of $\text{Ca}_3(\text{PO}_4)_2$ appears in the hydration products.

3.4.3 SEM analysis

SEM was used to observe the morphological structure and distribution characteristics of hydration products of CA paste samples with different curing ages. The observation results are shown in Figure 10. It can be seen that with the increase in curing age, more hydration products are generated. After 28 d of hydration, it is observed that the grain of ettringite gradually becomes coarser, the crystallinity increases, and the structure is rod-like. AFt and C-S-H gels interlace with each other to improve the compactness of the matrix, which is shown as a significant increase in flexural and compressive strength. Figure 10A shows

the SEM images of the CA with 3 d age. Hydration products have been produced in net paste samples at 3 d age. Under low magnification, dense C-S-H gel is found. However, there are still large, unhydrated particles exposed out of the C-S-H gel. Figure 10B indicates that there are fibrous AFt crystals and crystal sparse C-S-H gel grown across the gaps of the CA. Figures 10C, D show that at the 7 d age, there are flaky C-S-H gel and the acicular AFt crystals filling their internal pores. Figure 10E reveals the flocculent C-S-H gel at the 28 d age. Loose small particles have disappeared, and acicular AFt crystals exist in the cracks and crevices of the gel (Li F et al., 2020). As shown in Figure 10F, AFt crystals overgrow in the large cavity. With the continuous formation of the C-S-H gel and AFt crystals, the network structure is consolidated, increasing the CA filling material's macroscopic strength.

3.4.4 FI-IR analysis

In order to verify that the added material participated in the hydration reaction and generated the hydration products mainly composed of C-S-H gels and ettringite, FT-IR was used to infer the diffraction peaks of the hydration products. FT-IR analysis of CA paste samples is given in Figure 11. As can be seen from the figure, C-S-H gels and AFt stably existed after the material underwent hydration reaction. With the increase in curing time, hydration products increased, which was conducive to improving the mechanical properties of the cementing material. It can be seen that there is no significant difference in the FT-IR spectra of the CA samples at 3 d, 7 d, and 28 d of hydration, except for a slight decrease in transmittance near the wave number of 3,425, 1,090, 990, and 459 cm^{-1} . The absorption band at 3,425 cm^{-1} indicates the asymmetric stretching vibration

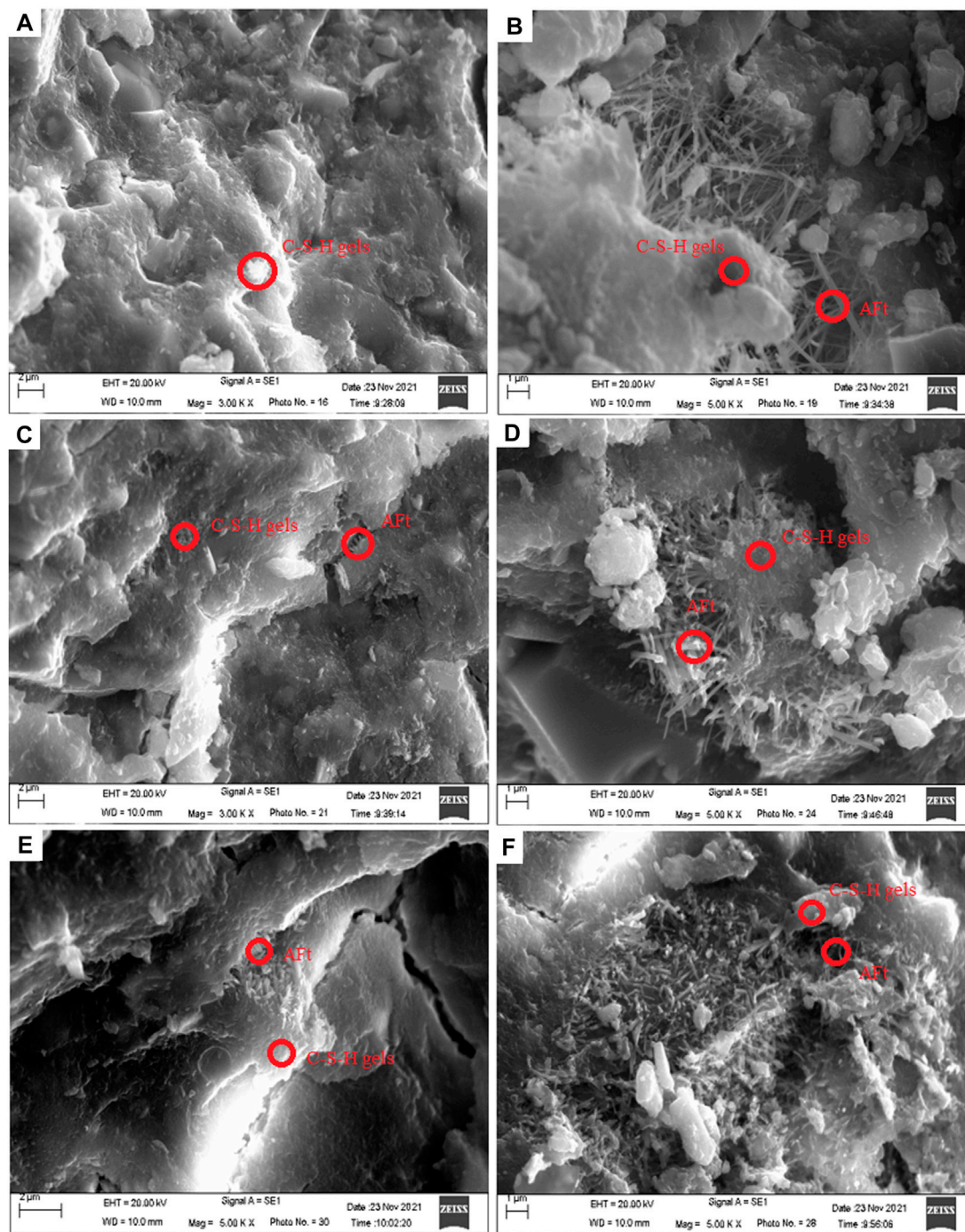


FIGURE 10
SEM images of CA paste samples at different ages. (A) and (B) 3 d; (C) and (D) 7 d; (E) and (F) 28 d.

of OH^- (Figure 11A), while the band at $1,645\text{ cm}^{-1}$ represents the flexural vibration of OH^- , which are the absorption characteristics of internal vibration of crystal water (Li Y et al., 2020; Liang et al., 2021; Li et al., 2022). This indicates that the hydration reaction of CA produces a lot of gel or substances with crystal water. However, as the reaction progresses, the transmittance of the OH^- absorption band decreases, proving the gradual increase of hydrous substances.

The vibration peaks at 990, 518, and 450 cm^{-1} represent the asymmetric stretching vibration of Si-O(Al) , and the out-of-plane and in-plane flexural vibrations of Si-O , respectively. According to Clayden et al. (1999), Lecomte et al. (2006), and Hanna et al. (1995), the vibration frequency of SiQ^n is: SiQ^4 , $1,200\text{ cm}^{-1}$; SiQ^3 , $1,100\text{ cm}^{-1}$; SiQ^2 , 950 cm^{-1} ; SiQ^1 , 900 cm^{-1} ; SiQ^0 , 850 cm^{-1} . Q indicates the silicon-oxygen tetrahedra, and n refers to the number of bridge oxygen connecting each silicon-oxygen tetrahedra and other Si atoms.

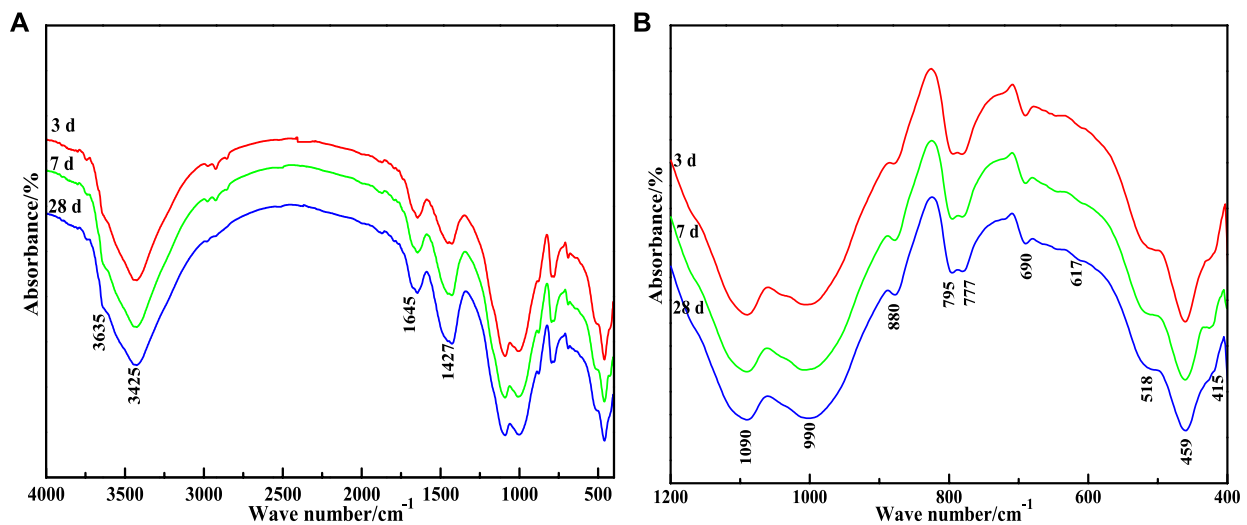


FIGURE 11 FT-IR patterns of CA paste samples at different ages. (A) 400–4000 cm^{-1} ; (B) 400–1200 cm^{-1}

The displacement of absorption peak shifts to lower wave numbers when the Si atoms in the silico-oxygen tetrahedra are replaced by the Al atoms in the sub adjacent coordination. Combined with Figure 11B, it can be concluded that the weak absorption peak of 880 cm^{-1} on the FT-IR map is attributed to SiQ^0 , which is the signal peak of insulated silicate in unhydrated SS and VTS. The strong absorption band near 990 cm^{-1} is attributed to the superposition of the chain silicate SiQ^2 phyllosilicate and SiQ^3 (mAl); The absorption peak near 1,090 cm^{-1} is attributed to the phyllosilicate SiQ^4 (mAl).

Figure 11B shows the amplification of the fingerprint region of CA paste samples FT-IR atlas (400–1,200 cm^{-1}). According to the report of Moon et al. (2012), it is speculated that most absorption peaks in the interval are characteristic absorption peaks of AFt. At 617 and 415 cm^{-1} is the flexural vibration of $[\text{SO}_4]^{2-}$; At 518 cm^{-1} is the absorption band of $[\text{AlO}_6]$ octahedron; The absorption band at 795 cm^{-1} is caused by the solid solution of AFt crystal with other elements which may be Fe, Si, and other elements.

4 Conclusion

In this paper, steel slag (SS), vanadium-titanium slag (VTS) and vanadium-titanium iron ore tailings (VTIOTs) were used as the main raw materials to make the mine cemented paste backfill material (CPBM). Through the research on its composition, properties, and hydration mechanism, it can be concluded that:

- (1) When the specific surface areas of SS and VTS are both 510 $\text{m}^2 \text{kg}^{-1}$, the CA composed of DWS, PG, and CPA can be used as the mine filling agent. Using the metallurgical waste SS and VTS as the cementing agent costs less than cement, and its environmental and ecological benefits are in line with national industrial policies.
- (2) The optimal mix proportion of CA is SS: VTS: PG: DWS = 31:59:6:4. Then, add into CPA which accounts for 4% of the mass of CA.

Further, prepare the filling materials with the cement sand ratio as 1:4, the PMC as 80%, and PC as 0.18% of the total CA. The slump value is 216 mm, and the 28 d flexural strength and compressive strength of CPBM reach 4.25 and 9.41 MPa, respectively, which meets the requirements of Chinese National Standard GB/T 39489-2020 Technical specification for the total tailings paste backfill.

- (3) Through the analysis of hydration heat, XRD, SEM and FT-IR, it is found that the heat release of the CA with the hydration of 60 h is less than 60% of the cement. The hydration products of the CA are mainly AFt crystals and C-S-H gel. The addition of CPA promotes the hydration of active minerals in SS and VTS. The SO_4^{2-} of PG accelerates the formation of AFt which further facilitates the fracture of $[\text{AlO}_4]^{5-}$ and $[\text{SiO}_4]^{4-}$ along the bridge oxygen in VTS and SS. Therefore, C-S-H gel is formed and deposited in the slurry solution with rich Ca^{2+} , gradually thickening and hardening the slurry.

Data availability statement

The raw data supporting the conclusion of this article will be made available by the authors, without undue reservation.

Author contributions

QY proposes method and writes manuscript; WC and ZhoY propose and participates in design research and reviews paper; JJ, MJ, PH, ZheY, ZhaY, and LF participate in design research and reviews paper. All the authors approved the final version of the manuscript.

Funding

The authors gratefully acknowledge financial support by the National Key Research and Development Program of China (No.

2021YFC1910605), the Natural Science Foundation of Hebei Province (E2020402079), State Key Laboratory of Solid Waste Resource Utilization and Energy Conservation (SWR-2023-007), Science and Technology Research and Development Plan of China Railway Construction Group Co., Ltd. (No. 22-11b, 22-14b), Handan Science and Technology Research and Development Program (21422111260). The funder was not involved in the study design, collection, analysis, interpretation of data, the writing of this article or the decision to submit it for publication.

Conflict of interest

Author YuZ and FL were employed by China Railway Construction Group Co., Ltd.

The remaining authors declare that the research was conducted in the absence of any commercial or financial

relationships that could be construed as a potential conflict of interest.

Publisher's note

All claims expressed in this article are solely those of the authors and do not necessarily represent those of their affiliated organizations, or those of the publisher, the editors and the reviewers. Any product that may be evaluated in this article, or claim that may be made by its manufacturer, is not guaranteed or endorsed by the publisher.

Supplementary material

The Supplementary Material for this article can be found online at: <https://www.frontiersin.org/articles/10.3389/feart.2023.1181952/full#supplementary-material>

References

- Ashrit, S., Chatti, R. V., and Udpa, K. N. (2017). An infrared and Raman spectroscopic study of yellow gypsum synthesized from LD slag fines. *MOJ Min. Metall.* 1 (1), 1–4.
- Bensted, J., and Barnes, P. (2002). *Structure and performance of cements*. New York: Sporn Press.
- Cho, B., and Choi, H. (2016). Physical and chemical properties of concrete using GGBFS-KR slag-gypsum binder. *Constr. Build. Mat.* 123, 436–443. doi:10.1016/j.conbuildmat.2016.07.023
- Cihangir, F., and Akyol, Y. (2018). Mechanical, hydrological and microstructural assessment of the durability of cemented paste backfill containing alkali-activated slag. *Int. J. Min. Reclam. Env.* 32 (2), 123–143. doi:10.1080/17480930.2016.1242183
- Clayden, N. J., Esposito, S., Aronne, A., and Pernice, P. (1999). Solid state ²⁷Al NMR and FTIR study of lanthanum aluminosilicate glasses. *J. Non-Cryst. Solids* 258 (1–3), 11–19. doi:10.1016/S0022-3093(99)00555-4(99)00555-4
- Cui, X., Ni, W., and Ren, C. (2017). Hydration mechanism of all solid waste cementitious materials based on steel slag and blast furnace slag. *Chin. J. Mat. Res.* 31 (9), 687–694. doi:10.11901/1005.3093.2016.741
- Deng, D., Liu, L., Yao, Z., Song, K., and Lao, D. (2017). A practice of ultra-fine tailings disposal as filling material in a gold mine. *J. Environ. Manage.* 196, 100–109. doi:10.1016/j.jenvman.2017.02.056
- Duan, S., Liao, H., Cheng, F., Song, H., and Yang, H. (2018). Investigation into the synergistic effects in hydrated gelling systems containing fly ash, desulfurization gypsum and steel slag. *Constr. Build. Mat.* 187, 1113–1120. doi:10.1016/j.conbuildmat.2018.07.241
- Fisher, L. V., and Barron, A. R. (2019). The recycling and reuse of steelmaking slags-A review. *Resour. Conserv. Recy.* 146, 244–255. doi:10.1016/j.resconrec.2019.03.010
- Ghirian, A., and Fall, M. (2016). Strength evolution and deformation behaviour of cemented paste backfill at early ages: Effect of curing stress, filling strategy and drainage. *Int. J. Min. Sci. Technol.* 26 (5), 809–817. doi:10.1016/j.ijmst.2016.05.039
- Hanna, R. A., Barrie, P. J., Cheeseman, C. R., Hills, C. D., Buchler, P. M., and Perry, R. (1995). Solid state ²⁹Si and ²⁷Al NMR and FTIR study of cement pastes containing industrial wastes and organics. *Cem. Concr. Res.* 25 (7), 1435–1444. doi:10.1016/0008-8846(95)00138-3
- Huo, B., Li, B., Chen, C., and Zhang, Y. (2021a). Mechanism and properties of glacial acetic acid modified steel slag powder via dry chemical modification method. *J. Chin. Ceram. Soc.* 49 (5), 948–954. doi:10.1016/j.jclevpro.2018.01.172
- Huo, B., Li, B., Chen, C., Zhang, Y., and Wang, D. (2021b). Morphological and mineralogical insights into acetic acid modifying and hydraulic process on steel slag for enhanced reactivity. *Constr. Build. Mat.* 307, 125004. doi:10.1016/j.conbuildmat.2021.125004
- Huo, B., Li, B., Huang, S., Chen, C., Zhang, Y., and Banthia, N. (2020). Hydration and soundness properties of phosphoric acid modified steel slag powder. *Constr. Build. Mat.* 254, 119319. doi:10.1016/j.conbuildmat.2020.119319
- Jiang, L., Li, C., Wang, C., Xu, N., and Chu, H. (2018). Utilization of flue gas desulfurization gypsum as an activation agent for high-volume slag concrete. *J. Clean. Prod.* 205, 589–598. doi:10.1016/j.jclevpro.2018.09.145
- Ke, X., Hou, H., Zhou, M., Yang, Y., and Zhou, X. (2015). Effect of particle gradation on properties of fresh and hardened cemented paste backfill. *Constr. Build. Mat.* 96, 378–382. doi:10.1016/j.conbuildmat.2015.08.057
- Leconte, I., Henrist, C., Liègeois, M., Masen, F., Rulmont, A., and Cloots, R. (2006). (Micro-)structural comparison between geopolymers, alkali-activated slag cement and Portland cement. *J. Eur. Ceram. Soc.* 26 (16), 3789–3797. doi:10.1016/j.jeurceramsoc.2005.12.021
- Li, F., Liu, L., Liu, K., Zheng, A., and Liu, J. (2020). Investigation on waterproof mechanism and micro-structure of cement mortar incorporated with silicane. *Constr. Build. Mat.* 239, 117865. doi:10.1016/j.conbuildmat.2019.117865
- Li, H., Liu, Y., Xu, C., Guan, X., Zou, D., and Jing, G. (2022). Synergy effect of synthetic ettringite modified by citric acid on the properties of ultrafine sulfoaluminat cement-based materials. *Cem. Concr. Compos.* 125, 104312. doi:10.1016/j.cemconcomp.2021.104312
- Li, N., Farzadnia, N., and Shi, C. (2017). Microstructural changes in alkali-activated slag mortars induced by accelerated carbonation. *Cem. Concr. Res.* 100, 214–226. doi:10.1016/j.cemconres.2017.07.008
- Li, W., and Fall, M. (2016). Sulphate effect on the early age strength and self-desiccation of cemented paste backfill. *Constr. Build. Mat.* 106, 296–304. doi:10.1016/j.conbuildmat.2015.12.124
- Li, W., Zhou, X., Liao, M., and Lin, Q. (2011). Research and practice on replacement materials for cementing backfilling. *Min. Eng.* 11 (3), 19–23. doi:10.13828/j.cnki.cjks.2011.03.025
- Li, Y., Qiao, C., and Ni, W. (2020). Green concrete with ground granulated blast-furnace slag activated by desulfurization gypsum and electric arc furnace reducing slag. *J. Clean. Prod.* 269, 122212. doi:10.1016/j.jclevpro.2020.122212
- Li, Y., Min, X., Ke, Y., Chai, L., Shi, M., Tang, C., et al. (2018). Utilization of red mud and Pb/Zn smelter waste for the synthesis of a red mud-based cementitious material. *J. Hazard. Mat.* 34, 343–349. doi:10.1016/j.jhazmat.2017.10.046
- Liang, G., Ni, D., Li, H., Dong, B., and Yang, Z. (2021). Synergistic effect of EVA, TEA and C-S-Hs-PCe on the hydration process and mechanical properties of Portland cement paste at early age. *Constr. Build. Mat.* 272, 121891. doi:10.1016/j.conbuildmat.2020.121891
- Mason, B. (1944). The constitution of some open-heart slag. *J. Iron Steel Res. Int.* 179 (11), 69.
- Mejdi, M., Wilson, W., Saillio, M., Chaussadent, T., Divet, L., and Tagnit-Hamou, A. (2019). Investigating the pozzolanic reaction of post-consumption glass powder and the role of portlandite in the formation of sodium-rich C-S-H. *Cem. Concr. Res.* 123, 105790. doi:10.1016/j.cemconres.2019.105790
- Moon, J., Oh, J. E., Balonis, M., Glasser, F. P., Clark, S. M., and Monterro, P. J. M. (2012). High pressure study of low compressibility tetracalcium aluminum carbonate hydrates 3CaO·Al₂O₃·CaCO₃·11H₂O. *Cem. Concr. Res.* 42 (1), 105–110. doi:10.1016/j.cemconres.2011.08.004
- Peyronnard, O., and Benzaazoua, M. (2012). Alternative by-product based binders for cemented mine backfill: Recipes optimisation using Taguchi method. *Min. Eng.* 29, 28–38. doi:10.1016/j.mineng.2011.12.010
- Su, L., and Zhang, X. (2013). Coordinated development between mineral resource exploitation and environmental protection with backfill technology. *Min. Metall. Eng.* 33 (3), 117–121. doi:10.3969/j.issn.0253-6099.2013.03.032
- Wang, C., Ni, W., Zhang, S., Wang, S., Gai, G., and Wang, W. (2016). Preparation and properties of autoclaved aerated concrete using coal gangue and iron ore tailings. *Constr. Build. Mat.* 104, 109–115. doi:10.1016/j.conbuildmat.2015.12.041

- Wang, C., Ren, Z., Huo, Z., Zheng, Y., Tian, X., Zhang, K., et al. (2021). Properties and hydration characteristics of mine cemented paste backfill material containing secondary smelting water-granulated nickel slag. *Alex. Eng. J.* 60 (6), 4961–4971. doi:10.1016/j.aej.2020.12.058
- Wang, C., Zhang, K., Zuo, W., Ye, P., Zhao, G., Ren, Z., et al. (2020). Preparation and properties of autoclaved aerated concrete using coal gangue and fly ash. *Mat. Rep.* 34 (12), 24034–24039. doi:10.13225/j.cnki.jccs.2013.0551
- Wang, F., Zheng, Q., Zhang, G., Wang, C., Cheng, F., and Lin, G. (2020). Preparation and hydration mechanism of mine cemented paste backfill material for secondary smelting water-granulated nickel slag. *J. New Mat. Electr. Sys.* 23 (1), 51–59. doi:10.14447/jnmes.v23i1.a10
- Wang, S., Wang, C., Wang, Q., Liu, Z., Qian, W., Jin, C., et al. (2018). Study on cementitious properties and hydration characteristics of steel slag. *Pol. J. Environ. Stud.* 27 (1), 357–364. doi:10.15244/pjoes/74133
- Wu, M., Zhang, Y., Jia, Y., Sha, W., Liu, G., Yang, Z., et al. (2019). Effects of sodium sulfate on the hydration and properties of lime-based low carbon cementitious materials. *J. Clean. Prod.* 220, 677–687. doi:10.1016/j.jclepro.2019.02.186
- Wu, Q., Wu, Y., Tong, W., and Ma, H. (2018). Utilization of nickel slag as raw material in the production of Portland cement for road construction. *Constr. Build. Mat.* 193, 426–434. doi:10.1016/j.conbuildmat.2018.10.109
- Yilmaz, E., Belem, T., and Benzaazoua, M. (2014). Effects of curing and stress conditions on hydromechanical, geotechnical and geochemical properties of cemented paste backfill. *Eng. Geol.* 168, 23–37. doi:10.1016/j.enggeo.2013.10.024
- Yilmaz, E., Belem, T., Bussière, B., Mbonimpa, M., and Benzaazoua, M. (2015). Curing time effect on consolidation behaviour of cemented paste backfill containing different cement types and contents. *Constr. Build. Mat.* 75, 99–111. doi:10.1016/j.conbuildmat.2014.11.008
- Yilmaz, T., Ercikdi, B., Karaman, K., and Külekçi, G. (2014). Assessment of strength properties of cemented paste backfill by ultrasonic pulse velocity test. *Ultrasonics* 54 (5), 1386–1394. doi:10.1016/j.ultras.2014.02.012
- Zhang, G., Wu, P., and Gao, S. (2019a). Properties and microstructure of low-carbon whole-tailings cemented paste backfill material containing steel slag, granulated blast furnace slag and flue gas desulphurization gypsum. *Acta Microsc.* 28 (4), 770–780.
- Zhang, G., Wu, P., Gao, S., Zhang, K., Wang, C., Huo, Z., et al. (2019b). Preparation of environmentally friendly low autogenous shrinkage whole-tailings cemented paste backfill material from steel slag. *Acta Microsc.* 28 (5), 961–971.
- Zhang, J., He, W., Ni, W., Hu, W., Chen, J., Zhu, T., et al. (2016). Research on the fluidity and hydration mechanism of mine backfilling material prepared in steel slag gel system. *Chem. Eng. Trans.* 51, 1039–1046. doi:10.11817/j.issn.1672-7347.2016.10.005
- Zhang, Q., Ji, T., Yang, Z., Wang, C., and Wu, H. (2020). Influence of different activators on microstructure and strength of alkali-activated nickel slag cementitious materials. *Constr. Build. Mat.* 235, 117449. doi:10.1016/j.conbuildmat.2019.117449
- Zhao, J., Wang, D., Yan, P., Zhang, D., and Wang, H. (2016). Self-cementitious property of steel slag powder blended with gypsum. *Constr. Build. Mat.* 113, 835–842. doi:10.1016/j.conbuildmat.2016.03.102